Nanoscale Current Spreading Analysis in Solution-Processed Graphene Oxide / Silver Nanowire Transparent Electrodes via Conductive Atomic Force Microscopy

Joseph E. Shaw,[1] Ajay Perumal,[1,2] Donal D. C. Bradley,[1,3] Paul N. Stavrinou,[1] and Thomas D. Anthopoulos[1,a)]

[1]*Department of Physics and Centre for Plastic Electronics, Blackett Laboratory, Imperial College London, SW7 2AZ, UK*

[2]*Present Address: Luminous! Centre of Excellence for Semiconductor Lighting and Displays, School of Electrical and Electronic Engineering, Nanyang Technological University Nanyang Avenue , Singapore 639798, Singapore*

[3]*Present Address: University of Oxford, Departments of Engineering Science and Physics, Mathematical, Physical and Life Sciences Division, 9 Parks Road, Oxford, OX1 3PD, UK*

We use conductive atomic force microscopy (CAFM) to study the origin of long-range conductivity in model transparent conductive electrodes composed of networks of reduced graphene oxide (rGO_X) and silver nanowires (AgNW), with nanoscale spatial resolution. Pristine networks of rGO_X (1-3 monolayers-thick) and AgNWs exhibit sheet resistances of ~100-1000 kΩ/□, and 100-900 Ω/□, respectively. When the materials are deposited sequentially to form bilayer rGO_X/AgNW electrodes and thermally annealed at 200 °C, the sheet resistance reduces by up to 36% as compared to pristine AgNW networks. CAFM was used to analyze the current spreading in both systems in order to identify the nanoscale phenomena responsible for this effect. For rGO_X networks the low intra-flake conductivity and the inter-flake contact resistance is found to dominate the macroscopic sheet resistance, while for AgNW networks the latter is determined by the density of the inter-AgNW junctions and their associated resistance. In the case of the bilayer rGO_X/AgNWs networks, rGO_X flakes are found to form conductive "bridges" between AgNWs. We show that these additional nanoscopic electrical connections are responsible for the enhanced macroscopic conductivity of the bilayer rGO_X/AgNW electrodes. Finally, the critical role of thermal annealing on the formation of these nanoscopic connections is discussed.

[a)]Author to whom correspondence should be addressed. Electronic mail: t.anthopoulos@ic.ac.uk

I. INTRODUCTION

The emergence of new forms of electronic materials such as carbon-based systems, metal oxides, and metal nanowires in the last decade has enabled the development of transparent and flexible electronics that can be solution processed using inexpensive techniques over large-area substrates at low temperatures.[1, 2] Indium tin oxide (ITO) is the most common and widely used transparent conductor, however, diminishing supplies and rising prices of indium have prompted significant research on alternative transparent electrode material systems.[3, 4] Silver nanowires (AgNWs), in particular, have attracted significant interest as a possible replacement for ITO due to silver's high conductivity (6.3×10^7 S/m)[5] and the well-established synthetic routes available.[6] To this end, AgNW electrodes have already been successfully utilized as transparent electrodes in a range of low-end applications including, solar cells,[7-9] touch screens[10-12] and organic light-emitting diodes (OLEDs).[13-16] One unique characteristic of AgNWs is that they combine the inherently high electrical conductivity of metals with the solution processing characteristics of organic-based materials. The combination of these attractive attributes enables deposition of highly transparent and electrically conductive layers on arbitrary substrate materials over large areas using inexpensive and scalable deposition techniques.

AgNWs are generally deposited onto substrates from suspensions using various methods including, spincoating,[17, 18] spraying,[16, 19-22] and wire bar coating.[5] In such nanoscopic networks, the macroscopic conductivity of the resulting electrode is limited by the percolating properties of the network, which it is in turn dictated by the nanowire's geometry and their density on the substrate's surface.[23,24] In the case of AgNWs, such resistive loses can be greatly reduced through post-deposition process steps such as thermal and electrical annealing,[24-27] as well as application of high pressure.[25] Alternatively, the AgNW networks can be combined with sequentially deposited interlayer materials such as hole injecting interlayers, which can both

assist with the tuning of the electrode's microscopic work function as well as reduce its sheet resistance due to their role as conductive binder material.[16] AgNWs networks are also known for their poor adhesion to most substrate materials, which leads to relatively poor mechanical stability which is important, although not critical, for use in large area electronics.[5] A further potential disadvantage of AgNW networks is that their electrical conductivity can degrade upon exposure to air, primarily due to nanowire surface oxidation.[28, 29]

One approach that has been shown to improve the stability and performance of conductive AgNW networks is by blending the nanowires with a semi/conductive binder material.[6] The latter method has been shown to increase both the mechanical stability and conductivity of the network.[5, 30-33] Although the nanoscopic origin of the latter is still debatable, different theories have been put forward to explain the experimental results. Chen et al., proposed that the conductive binder aids charge transport between nanowires with an overall positive impact on the network's macroscopic conductivity.[30] Zhu et al. on the other hand argued that upon solution-deposition and thermal annealing, evaporation of the solvent used to dissolve the binder material produces capillary forces that draw the AgNWs closer together, decreasing the inter-AgNWs junction resistance and hence reducing the macroscopic sheet resistivity of the network.[34] However, synergistic effects of these, or more, effects may well be at work and cannot be fully disregarded at this point.

Another binder/interlayer material system that has been proposed recently is graphene oxide (GO_X), a solution processable two-dimensional material with relatively high conductivity and appreciable charge carrier mobility.[35, 36] Unlike graphene, however, GO_X contains a large number of lattice defects that are populated by oxide/hydroxide groups that act as charge traps and contribute to its inferior electrical performance. However, the presence of these

oxide/hydroxide surface groups render GO_X more hydrophilic and hence easier to process onto large-area substrates than solutions of exfoliated graphene.[5] This advantageous characteristic is the primary reason why interest in using GO_X in transparent conductive electrodes continues to increase.[37-40] Importantly, GO_X can be converted to the more conductive form of reduced graphene oxide (rGO_X) via thermal annealing or chemical treatment.[41] Although conversion of GO_X to rGO_X decreases the density of hydroxyl groups, a significant density of structural defects remains. As a result the conductivity of rGO_X is well below that of pristine graphene.[41]

Recently, several groups have reported the occurrence of strong electrostatic interactions between AgNWs and graphene-based materials.[5, 42, 43] The apparent compatibility between the two systems has led to the development of transparent and flexible rGO_X/AgNW nano-composite electrodes and devices.[5, 29-32, 44] Combination of rGO_X and metal nanowires in bilayer configuration has also been shown to improve the mechanical and chemical stability of the electrode[5, 31] while improving its macroscopic conductivity.[29-31, 44, 45] Despite the great promise, however, to date there has been no in-depth analysis of the nano-scale phenomena responsible for the increased conductivity in such hybrid networks. Understanding these phenomena may well hold the key for future developments in this field and as such demand further attention.

Here, we use lateral conductive atomic force microscopy (CAFM) to study the current spreading in pristine (rGO_X, AgNW) and bilayer rGO_X/AgNW networks, with nanometer resolution. Particular emphasis is placed on the bilayer electrodes comprised of AgNWs deposited onto 1-3 monolayers-thick rGO_X networks. Lateral CAFM measurements reveal the key role of rGO_X flakes on the formation of inter-AgNW electrical connections upon thermal annealing at 200 °C. On the basis of these results we propose that the presence of these nano-

scale rGO_X-mediated conductive "bridges" formed between AgNWs is primarily responsible for the significant increase in the macroscopic conductivity of the rGO_X/AgNW electrodes.

II. METHODS

Networks of rGO_X, AgNW and rGO_X/AgNW were characterized using optical transmission and electrical sheet resistance measurements. Quartz substrates were used for optical transmission measurements while sheet resistance analysis was performed on layers processed on doped Si^{++} wafers with a thermally grown 400 nm-thick layer of SiO_2 acting as the insulator. CAFM measurements were performed using the same Si^{++}/SiO_2 substrates equipped with thermally evaporated Au electrodes acting as the remote electrodes. Prior to rGO_X and AgNW deposition, substrates were subjected to UV/ozone for 10 minutes to remove unwanted contaminants.

Graphene oxide (GO_X) was purchased from Graphene Supermarket (6 mg/ml in H_2O) and was diluted to 0.5 mg/ml in H_2O. GO_X dispersions were then spin-coated onto the cleaned substrates at 1300 rpm for 2 min resulting to the formation of 1-3 monolayers-thick GO_X networks. Reduced GO_X (rGO_X) was obtained by thermal annealing the GO_X networks in nitrogen at 200 °C for 1 h.

Ethanol-based AgNW dispersions were purchased from Blue Nano at an initial suspension concentration of 10 mg/ml. The dispersions were then diluted to varying concentrations and spin-coated at 2000 rpm for 1 min in ambient air. As-deposited AgNW networks were then annealed in nitrogen at 200 °C for 1 h. rGO_X/AgNW bilayer networks were grown by depositing first a 1-3 monolayer-thick GO_X network and thermally annealing it at 200 °C for 1 h in nitrogen, followed by the deposition of the AgNW dispersion. The resulting bilayer rGO_X/AgNW networks were finally annealed at 200 °C for 1 h in nitrogen.

CAFM measurements were performed using an Agilent 5500 AFM system in CAFM mode using a Ti/Pt conductive tip purchased from MikroMasch. The CAFM mode operated at a bias range of ±10 V with an imaging current saturation level of ±10 nA. Electrical connection between the Au electrode and the ground terminal was made using a fine copper wire using conductive silver paste. Detailed description of the sample geometry used for the CAFM measurements is provided in Section IV.

Sheet resistance measurements were performed using a high-accuracy four-point-probe measurement system (Jandel RM3000) at a constant current supply of 100 μA. Tungsten probes with a diameter of 100 μm and inter-probe spacing of 1 mm were employed. The Jandel RM3000 system combines a constant current source with a digital voltmeter and is designed to perform resistivity measurements while a constant force is applied between the four-point-probe head and the sample.

Ultraviolet-visible (UV-Vis) transmittance measurements in the range of 200-900 nm were recorded with a Shimadzu UV-2600 spectrophotometer equipped with an ISR-2600Plus integrating sphere. Both transmission and reflection spectra were recorded to allow the correct calculation of absorption (A) using the formula $A = \log(T/(1-R))$, where T and R are the transmittance and reflectance, respectively.

III. ELECTRICAL SHEET RESISTANCE ANALYSIS

Prior to CAFM measurements, we assessed the electrical sheet resistance and optical transmittance properties of pristine rGO_X and AgNW networks and compared the results to the sheet resistance and transmittance of the composite bilayer rGO_X/AgNW systems. The resulting

rGO_X networks exhibit high optical transmittance (92.6 % at 550 nm) and a sheet resistance in the range of 100-1000 kΩ/□. Although this is still a relatively high value, it is significantly lower than the sheet resistance of as-processed GO_X layers (>5×10^8 Ω/□) highlighting the benefits of thermal reduction under inert atmosphere. Networks of AgNWs were spin-coated from solutions of different concentrations onto quartz substrates and annealed at 200 °C in nitrogen. Analysis of the formed networks by AFM and optical microscopy methods reveal the presence of AgNWs with lengths and diameters in the range of 10-100 μm and 100-200 nm, respectively. **Figure 1(a)** shows an optical microscope image of a representative AgNW network after thermal annealing, while **Figure S1** shows optical images of similar networks of varying density.

Bilayer rGO_X/AgNW electrodes were produced via the two-step deposition process described in the *Methods* section. The average sheet resistance values of pristine AgNW networks and bilayer rGO_X/AgNW electrodes, for different AgNW network densities, are displayed in **Figure 1(b)** as a function of optical transmittance at 550 nm. The density of the AgNW networks was varied by altering the concentration of the AgNW dispersion. It can be seen that the sheet resistance in both electrode systems appears to increase with decreasing AgNW density in agreement with previously published data.[28] Interestingly, the bilayer rGO_X/AgNW systems exhibit a consistently lower sheet resistance (higher conductivity) than pristine AgNW networks for all nanowire densities. The incorporation of the 1-3 monolayer-thick rGO_X network has a small effect on the electrode's optical transmittance as it is found to decrease by approximately 0.6 % or less. On plotting individual trend-lines through each of the two data sets in **Figure 1(b)**, one can see that even after factoring in the slight decrease in the transmittance due to the rGO_X absorption, the bilayer rGO_X/AgNW electrodes exhibit lower sheet resistance across the entire transmittance range investigated. The positive impact of rGO_X is more prominent for dispersed AgNW networks since the characteristic sheet resistance is

found to reduce from 862 Ω/□ to 547 Ω/□ (~36 %) as compared to denser AgNW networks where it reduces by only ~24 % (from ~102 Ω/□ to ~77 Ω/□). These findings are in accordance with previously published results for similar materials combinations.[29-31, 44, 45]

IV. CURRENT SPREADING ANALYSIS BY CAFM

The origin of the reduced sheet resistance measured in rGO_X/AgNW electrodes was further investigated using lateral CAFM, a method which has been used to a great effect in the analysis of charge transport within a variety of materials including polymer and small molecule materials,[46, 47] and two-dimensional conductive materials such as graphene and MoS_2.[48, 49] **Figure 2(a)** shows the schematic of the CAFM measurement setup used to characterized the pristine rGO_X and AgNW networks as well as the bilayer rGO_X/AgNW networks. The CAFM measurements were performed by scanning the biased conductive AFM probe (AFM tip coated with Pt/Ir) over the network and continuously recording the current and surface topography (height) as a function of x-y position. Using these data we can then compose a current map and the surface topography of the conductive network.

The topography and current map images for a dilute network of AgNWs in proximity to the lateral Au electrode are shown in **Figure 2(b)** and **2(c)**, respectively. In the topography image AgNWs that are physically isolated (indicated by the dashed box) from the AgNW network and the Au electrode, are visible. The impact of this physical isolation can clearly be seen in the current map of **Figure 2(c)** (recorded at 1.6 V) where the isolated AgNWs are now invisible since they do not contribute to the current flow in the network. Instead, only the electrically "active" AgNWs, i.e. nanowires that are electrically connected to the network/Au electrode, are

visible. Although simple, the method is very powerful and provides direct information of the current conducting (percolating) pathways that govern the macroscopic conductivity of the network.

Figure 2(d) displays the cross-sections of an AgNW obtained from the topography data in **Figure 2(b**). By assuming that the cross-section of the AgNWs is circular, the diameter of the AgNWs can be approximated directly from the topography data yielding a value in the range of 150-170 nm. We note however that AgNWs with slightly different diameters are also present making estimation of the average diameter difficult. The broadening of the cross-section closer to the substrate is attributed to the AFM probe-imaging convolution and specifically the shape and size of the conductive tip. To this end the CAFM tip used here had a conical shape with a conductive apex diameter of approximately 30 nm. A similar observation was reported by Kim *et al.* for electrodes comprised of AgNWs and aluminum-doped ZnO.[33] Although, not critical for this work, such imaging effects may impose limitations in the ultimate spatial resolution achievable by the CAFM method, especially in samples with lateral surface features <30 nm, and the use of high aspect ratio conductive AFM tips is strongly recommended.

CAFM measurements were also performed on solution-processed rGO_X networks. The minimum rGO_X layer thickness, which reliably led to high substrate coverage, was found to be between 1-3 monolayers. **Figure 3(a)** shows the topography image for a representative rGO_X network. When the CAFM tip is biased at 5 V a clear current map is obtained highlighting the presence of the rGO_X flakes [**Figure 3**(**b)**]. Although the buried Au electrode is not visible in both the topography and current map images and is positioned approximately 5 μm off the right hand side of each scan window. **Figure 3(c)** shows a higher resolution current map for the rGO_X network while **Figure 3(d)** displays the topographical and current cross-sections (line scan)

taken from **Figure 3(c)** at the position indicated by the dashed line. In this image the Au electrode is located on the left hand side and it is not visible. The topographical cross-sections in **Figure 3(d)** show that the rGO_X network is composed of different numbers of monolayers with their approximate height/thickness indicated by the dotted lines. In **Figures 3(c)** and **(d)**, position 1 represents a two-monolayer rGO_X segment (~2 nm-thick) while position 2 is believed to be a three monolayers-thick segment of the network. Presence of voids on the current map, where no current is detected, are also evident and are most likely associated with network discontinuities due to incomplete surface coverage.

The CAFM line scan in **Figure 3(d)** reveals a steady decrease in measured current as the tip moves away from the edge of the Au electrode located on the left hand side of the image. Interestingly, the current level/profile within a single flake remains almost constant indicating efficient charge transport with small resistive losses. However, as the tip moves further way and across different rGO_X flakes, the measured current reduces in discrete steps. These changes take place either at the boundaries between adjacent rGO_X flakes or when there is a change in the number of monolayers. As the number of inter-flake boundaries increases, the current level tends to decrease i.e. from left to right. An example of the impact of this parasitic resistance is shown in **Figure 3(d)**, where the current measured between position 1 and position 2 reduces significantly from ~0.56 nA to ~0.36 nA even though the thickness of the network at position 2 is higher and equal to 3 monolayers. Based on these results we postulate that the main current limiting mechanism is the resistive nature of inter-flake boundaries and/or the nature/degree of inter-flake overlap(s).

By invoking Ohm's law, the inter-flake grain boundary (GB) resistance (evaluated at a tip-Au electrode bias of 5 V) is approximated to be on the order of ~5 GΩ. However, this rather

large inter-flake resistance value is neither representative nor constant as it depends on a number of factors including; the number of rGO_X layers, the extent of overlap between the two or more rGO_X flakes, and the nature of the inter-flake interaction(s).[50] To this end, it can be seen in **Figure 3(c)** that the electrical connectivity between different flakes ranges from high, identifiable by little or no change in the current level (shade), to highly resistive where GB resistivity values in the GΩ range are measured. However, we do note that Ohm's law may not be fully applicable and other possible contributions such as the occurrence of nonlinear "super-Joule" self-heating,[51] may also be at play. However, such analysis is indeed very challenging in the present sample geometry (CAFM) and certainly beyond the scope of this work.

Following on from the current-spreading analysis of pristine AgNW and rGO_X networks, networks consisting of rGO_X/AgNW bilayers were grown and analyzed via CAFM in an effort to identify the nanoscale phenomena responsible for the significant reduction in the macroscopic sheet resistance seen in **Figure 1(b)**. For this purpose two types of samples were prepared. The first type was produced by depositing a GO_X network and thermally reducing it to rGO_X followed by the deposition of the AgNWs by spin-coating. The electrodes were then dried at 80 °C for 20 min in order to remove remaining solvent followed by the CAFM measurements. The second type of sample consists of exactly the same bilayer rGO_X/AgNW structure but with the electrode being subjected to an additional and final annealing step at 200 °C for 1h in nitrogen.

Figure 4(a-b) show the topography and current map images for a bilayer network before annealing. The evaporated Au electrode can be seen on the right of the current map image (bright region). The latter is overlaid with rGO_X flakes [seen in **Figure 4(a)**], as well as two AgNWs positioned across the electrode's edge – one at the very bottom of the image. Close analysis of the current map in **Figure 4(b)** reveals the presence of GO_X flakes in close proximity to the Au

electrode edge. However, the measured current rapidly diminishes as the CAFM tip moves away from the Au electrode edge i.e. from right to left side of the image. This is believed to be the result of the combined effects of the low conductivity of GO_X flakes and the highly resistive nature of the inter-GO_X flake boundaries. As expected, the two AgNWs remain highly conductive in the current map, since they are electrically connected to the Au electrode either via direct physical contact, and/or through voids present in the GO_X network, and/or via quantum mechanical tunneling of charge carrier from the AgNW to the Au electrode through the GO_X flakes. Importantly, no current flow between the GO_X network and the AgNWs is evident. This feature is better illustrated in the current map of **Figure 4(b)** where an isolated AgNW highlighted in the left side of **Figure 4(a)** is not visible at all. This is attributed to the electrically insulating nature of the underlying GO_X network, which is not able to mediate charge transport between the AgNWs. Finally, **Figure 4(c)** displays the point current-voltage (I-V) characteristics obtained from two different positions on the bilayer electrode - one taken on the GO_X network (position 1), and one directly on the AgNWs (position 2) in **Figure 4(b)**. The very low current measured at position 1 is indicative of the highly resistive nature of the GO_X network, while the I-V taken at position 2 resembles short circuit due to the metallic nature of the AgNW. Only at tip biases >8 V does measurable current start flowing between AgNWs and GO_X flakes but only at regions in close proximity to the tips of the AgNWs (apexes). This unexpected effect is better illustrated in **Figures 4(d-e)** where only GO_X flakes in proximity to an AgNW apex appear to be electrically connected. There are two possible explanations for this observation. First, AgNWs may be lying slightly bowed on the substrate and/or lying across other nanowires therefore minimizing contact with the ultra-thin underlying GO_X network. Secondly, residue of the insulating polyvinylphenol (PVP) polymer often used during AgNW synthesis surrounds the surface of the AgNWs but not the apexes since the latter regions may have formed after

mechanical breaking of the initially longer nanowires during dispersion preparation (ultra-sonication). Although a very interesting observation, and potentially of critical importance, further work will be required to confirm or refute these proposals.

CAFM analysis was also performed after thermal annealing of the bilayer rGO_X/AgNW networks at 200 °C for 1h in nitrogen. **Figure 5(a)** displays the surface topography of a representative annealed rGO_X/AgNW network while **Figure 5(b)** shows the corresponding current map. Unlike un-annealed networks, extensive electrical connections between the sidewalls of the AgNWs and adjacent rGO_X flakes are now clearly visible. This is most likely the result of the removal of insulating residues (e.g. PVP)[52] from the AgNW's surface due to annealing. To this end, it is evident from **Figures 5(b)** that upon annealing, rGO_X flakes themselves contribute significantly to charge transport to/from the AgNWs by playing the role of conductive bridges in the macroscopic percolating AgNW network. As a result the macroscopic conductivity of the bilayer electrode increases.

Additional evidence of the key role of rGO_X is shown in **Figure 5(c)** where the I-V characteristics obtained after annealing from an isolated AgNW (position 1) -that is a nanowire connected to the Au electrode via rGO_X flakes- appear similar to that obtained from an rGO_X flake that is in direct contact with the remote Au electrode (position 2). The similarity in the current level and shape of the I-Vs is a direct consequence of the fact that in both cases rGO_X flakes mediate charge transport. In other words, rGO_X appears to dominate (i.e. limit) charge transport in the system since its conductivity is several orders of magnitude lower than that of AgNWs. Higher currents can only be measured by placing the CAFM tip in direct contact with the AgNW that is in direct contact with the Au electrode (position 3).

The key role of short-range current transport mediation by rGO_X between the two physically separated AgNWs shown in **Figure 5(d)** is illustrated in the current map of **Figure 5(e)**. Here one can observe the interesting occurrence of current flow from the apex of an AgNW that is in contact with the Au electrode, to an isolated AgNW through a small number of rGO_X flakes (highlighted region). Unlike non-annealed bilayer samples [**Figure 4(b)**], no preferential charge injection from the apexes of the AgNWs to the rGO_X flakes is observed. On the contrary, efficient current injection into rGO_X flakes at different positions along the AgNW length is evident [**Figure 5(e)**].

The same effect is better illustrated in the current map of **Figure 6** where an AgNW can be seen overlapping both a number of rGO_X flakes and the remote Au electrode located on the right hand side of the image. Although the current through the AgNW is very high, rGO_X flakes that are in direct contact with the nanowire can be seen to form additional electrical connections to the remote Au electrode (brighter regions). These results are of significant importance as they provide direct evidence of the critical role of rGO_X in creating additional electrical connections between the AgNWs as well as of the impact of thermal annealing. Although it has been previously hypothesized that the inclusion of a binder material such as rGO_X or graphene flakes acts as a conductive medium that enhances charge transport between AgNWs,[30] the present results represent the first direct evidence and lay the foundation for future studies.

In addition to reduced sheet resistance, incorporation of rGO_X provides numerous other advantages. For example, it reduces the amount of AgNWs required to achieve a given conductivity value while maintaining the high optical transparency. Since rGO_X is inexpensive as compared to AgNWs, it also offers the potential for significant reduction in materials cost. Furthermore, the presence of rGO_X flakes help to bridge voids that exist between metallic

nanowires. The latter is particularly relevant to device applications such as light-emitting diodes and organic photovoltaic cells where uniform charge injection/extraction from the active area of the electrode is of critical importance for achieving high power efficiencies.[30] These attributes make the rGO_X/AgNW electrode system highly attractive for applications in large-area, large-volume electronics. We therefore believe that the experimental evidence presented and analyzed here provide the basis on which previously reported results describing the conductivity evolution in AgNW and copper nanowire networks through the addition of rGO_X flakes, can now be explained.[31, 45]

V. SUMMARY AND CONCLUSIONS

We studied the conductivity of solution-deposited transparent electrodes comprised of randomly assembled networks of rGO_X, AgNWs and bilayer rGO_X/AgNW. When compared to pristine AgNW networks, bilayer rGO_X/AgNW systems are found to exhibit significantly reduced (24-36 %) sheet resistance while maintaining their high optical transparency (88-92 %). Pristine rGO_X networks on the other hand are found to be significantly more resistive (100-1000 kΩ/□) with charge transport being limited primarily by inter-flake (i.e. flake-to-flake) contact resistance. In order to elucidate the origin of the enhanced conductivity in rGO_X/AgNW networks, we have studied their electrical properties using a modified CAFM method. The latter allowed visualization of current spreading with nanometre lateral resolution, providing unique insights into the nanoscale transport phenomena responsible for the reduced sheet resistance observed as well as on key the role of thermal annealing. In particular, we showed that the incorporation of a randomly assembled network of rGO_X flakes as an underlying layer leads to the formation of additional electrical connections between subsequently deposited AgNWs, a

highly interesting and previously unreported phenomenon. The role of these nanoscopic connections is to increase the current flow in the macroscopic rGO_X/AgNW network without reducing its optical transparency. Thermal annealing of these randomly assembled bilayer networks was found to be of paramount importance in establishing, and further enhancing, the conductivity of these nanoscopic connections. On the basis of these findings we argue that similar transport phenomena maybe at play in other electrode systems composed of similar materials but prepared in different manner. Our work provides unique insights on the origin of the improved conductivity in rGO_X/AgNW electrodes, while the lateral CAFM data has emphasised the usefulness of the method as a tool for analysing the conductivity of model composite electrodes with nanoscale resolution. Importantly, the proposed lateral CAFM method is generic and could in principle be applied to other materials systems with significant implications on the analysis and development of next-generation transparent electrode technologies.

ACKNOWLEDGMENT

We acknowledge financial support from the Engineering and Physical Sciences Research Council (EPSRC) (grant EP/G037515/1). A.P. and D.D.C.B. also acknowledge support from the Imperial College EPSRC Impact Acceleration Account and D.D.C.B., T.D.A. and P.S. from the EPSRC Centre for Innovative Manufacturing in Large Area Electronics (grant EP/K03099X/1). D.D.C.B. further acknowledges the Lee-Lucas endowment.

FIGURE CAPTIONS

FIG. 1. (a) Dark field optical microscope image of AgNWs network spin-coated onto a quartz substrate. (b) Optical transmittance measured at 550 nm versus sheet resistance (Ω/□) for a pristine AgNWs and a bilayer rGO_X/AgNWs network after annealing at 200 °C in nitrogen.

FIG. 2. (a) Schematic of the conductive atomic force microscopy measurement set-up used. Topography (b) and current maps (c) obtained for an AgNW network at a tip bias of 1.6 V. The remote Au electrode is located on the right hand side of each image. (d) Topographical profile of an AgNW demonstrating broadening of the AgNW features in the images owing to AFM tip convolution.

FIG. 3. Topography (a) and corresponding current-map (b) images for a 1-3 monolayer-thickness rGO_X network. The current map was obtained with a tip bias set at 3.7 V. In (b) the Au electrode is not visible but it is located on the right hand side of the image. High-resolution current map (c) and the representative topography and current profiles (d) obtained from the line scan in (c) indicated with the white dashed line. In the current map of (c) and the current profile trace in (d), points 1 ➔ 2 indicate the current profile across an inter-flake boundary highlighting the significant drop in current. In (c) the remote Au electrode is located on the left hand side of the image. The current map in (c) was obtained with a tip bias of 5 V.

FIG. 4. (a-b) Topography and corresponding current maps obtained from a bilayer rGO_X/AgNWs electrode before being subjected to thermal annealing. The remote Au electrode is located on the on right hand side of the image. CAFM measurements were performed with a tip bias of 2 V. (c) Point current-voltage (I-V) characteristics measured at positions 1 and 2 indicated in (b). (d) Topography image of a bilayer GO_X/AgNWs network and the corresponding current map (e) showing preferential injection of current from the AgNW's apex to GO_X flakes (highlighted area). CAFM measurements in (e) were performed using a tip bias of 8 V.

FIG. 5. Topography image (a) and the corresponding current map (b) measured for a bilayer rGO_X/AgNWs electrode after it has been thermally annealed at 200 °C for 1h in nitrogen. The current map was obtained with a tip bias of 2 V. (c) Current-voltage (I-V) characteristics taken from the three different positions indicated in (b). The I-V curve measured at position 1 corresponds to an isolated AgNW that is only connected to the remote Au electrode via the rGO_X network. The I-V curve measured at position 2 results from charge transport through the rGO_X network itself, while the I-V at position 3 corresponds to current being transported through a single AgNW directly to the Au electrode. Further topography (d) and corresponding current map (e) images for another part of the bilayer rGO_X/AgNW network. The image shows a AgNW that is not connected directly to the remote Au electrode (located on the right hand side of the image). Despite this, electrical connections between the "isolated" AgNWs and adjacent rGO_X flakes can be seen along the length of the AgNW.

FIG. 6. Current map measured for a rGO_X/AgNWs electrode after has been annealed at 200 °C for 1 h under nitrogen. The current map reveals the current flow between rGO_X flakes located beneath the AgNW. The remote Au electrode is located on the right hand side of the image as indicated.

REFERENCES

1. T.W. Kelley, P.F. Baude, C. Gerlach, D.E. Ender, D. Muyres, M.A. Haase, D.E. Vogel, and S.D. Theiss, Chem. Mater. **16**, 4413 (2004).

2. S.R. Forrest, Nature **428**, 911 (2004).

3. K. Ellmer, Nat. Photonics **6**, 809 (2012).

4. D.S. Hecht, L. Hu, and G. Irvin, Adv. Mater. **23**, 1482 (2011).

5. Y.S. Yun, D.H. Kim, B. Kim, H.H. Park, and H.-J. Jin, Synth. Met. **162**, 1364 (2012).

6. D. Langley, G. Giusti, C. Mayousse, C. Celle, D. Bellet, and J.-P. Simonato, Nanotechnology **24**, 452001 (2013).

7. F.S.F. Morgenstern, D. Kabra, S. Massip, T.J.K. Brenner, P.E. Lyons, J.N. Coleman, and R.H. Friend, Appl. Phys. Lett. **99**, 183307 (2011).

8. J.-W. Lim, D.-Y. Cho, K. Eun, S.-H. Choa, S.-I. Na, J. Kim, and H.-K. Kim, Sol. Energy Mater. Sol. Cells **105**, 69 (2012).

9. W. Gaynor, J.-Y. Lee, and P. Peumans, ACS Nano **4**, 30 (2010).

10. A.R. Madaria, A. Kumar, and C. Zhou, Nanotechnology **22**, 245201 (2011).

11. J. Lee, P. Lee, H. Lee, D. Lee, S.S. Lee, and S.H. Ko, Nanoscale **4**, 6408 (2012).

12. W. Hu, X. Niu, R. Zhao, and Q. Pei, Appl. Phys. Lett. **102**, 083303 (2013).

13. L. Li, Z. Yu, W. Hu, C. Chang, Q. Chen, and Q. Pei, Adv. Mater. **23**, 5563 (2011).

14. W. Gaynor, S. Hofmann, M.G. Christoforo, C. Sachse, S. Mehra, A. Salleo, M.D. McGehee, M.C. Gather, B. Lüssem, L. Müller-Meskamp, P. Peumans, and K. Leo, Adv. Mater. **25**, 4006 (2013).

15. K.-K. Kim, S. Lee, H. Kim, J.-C. Park, S.-N. Lee, Y. Park, S.-J. Park, and S.-W. Kim, Appl. Phys. Lett. **94**, 071118 (2009).

16. S. Coskun, E. Selen Ates, and H.E. Unalan, Nanotechnology **24**, 125202 (2013).

17. C.-H. Chung, T.-B. Song, B. Bob, R. Zhu, and Y. Yang, Nano Res. **5**, 805 (2012).

18. D.-S. Leem, A. Edwards, M. Faist, J. Nelson, D.D.C. Bradley, and J.C. de Mello, Adv. Mater. **23**, 4371 (2011).

19. R.C. Tenent, T.M. Barnes, J.D. Bergeson, A.J. Ferguson, B. To, L.M. Gedvilas, M.J. Heben, and J.L. Blackburn, Adv. Mater. **21**, 3210 (2009).

20. Y.C. Lu and K.S. Chou, Nanotechnology **21**, 215707 (2010).

21. V. Scardaci, R. Coull, P.E. Lyons, D. Rickard, and J.N. Coleman, Small **7**, 2621 (2011).

22. A.R. Rathmell, S.M. Bergin, Y.-L. Hua, Z.-Y. Li, and B.J. Wiley, Adv. Mater. **22**, 3558 (2010).

23. D. Hecht, L. Hu, and G. Grüner, Appl. Phys. Lett. **89**, 133112 (2006).

24. S. De, T.M. Higgins, P.E. Lyons, E.M. Doherty, P.N. Nirmalraj, W.J. Blau, J.J. Boland, and J.N. Coleman, ACS Nano **3**, 1767 (2009).

25. T. Tokuno, M. Nogi, M. Karakawa, J. Jiu, T.T. Nge, Y. Aso, and K. Suganuma, Nano Res. **4**, 1215 (2011).

26. C. Celle, C. Mayousse, E. Moreau, H. Basti, A. Carella, and J.-P. Simonato, Nano Res. **5**, 427 (2012).

27. X.-Y. Zeng, Q.-K. Zhang, R.-M. Yu, and C.-Z. Lu, Adv. Mater. **22**, 4484 (2010).

28. X. Zhang, W.N.M. Wong, and M.M.F. Yuen, 23 (2012).

29. I.K. Moon, J. Il Kim, H. Lee, K. Hur, W.C. Kim, and H. Lee, Sci. Rep. **3**, 1 (2013).

30. R. Chen, S.R. Das, C. Jeong, M.R. Khan, D.B. Janes, and M. a. Alam, Adv. Funct. Mater. **23**, 5150 (2013).

31. I.N. Kholmanov, M.D. Stoller, J. Edgeworth, W.H. Lee, H. Li, J. Lee, C. Barnhart, J.R. Potts, R. Piner, D. Akinwande, J.E. Barrick, and R.S. Ruoff, ACS Nano **6**, 5157 (2012).

32. Q.T. Tran, T.M.H. Huynh, D.T. Tong, V.T. Tran, and N.D. Nguyen, Adv. Nat. Sci. Nanosci. Nanotechnol. **4**, 045012 (2013).

33. A. Kim, Y. Won, K. Woo, S. Jeong, and J. Moon, Adv. Funct. Mater. **24**, 2462 (2014).

34. R. Zhu, C.-H. Chung, K.C. Cha, W. Yang, Y.B. Zheng, H. Zhou, T.-B. Song, C.-C. Chen, P.S. Weiss, G. Li, and Y. Yang, ACS Nano **5**, 9877 (2011).

35. Y. Zhu, S. Murali, W. Cai, X. Li, J.W. Suk, J.R. Potts, and R.S. Ruoff, Adv. Mater. **22**, 3906 (2010).

36. F. Perrozzi, S. Prezioso, and L. Ottaviano, J. Phys. Condens. Matter **27**, 013002 (2015).

37. G. Eda, G. Fanchini, and M. Chhowalla, Nat. Nanotechnol. **3**, 270 (2008).

38. P.H. Wöbkenberg, G. Eda, D.-S. Leem, J.C. de Mello, D.D.C. Bradley, M. Chhowalla, and T.D. Anthopoulos, Adv. Mater. **23**, 1558 (2011).

39. X. Zhu, Y. Zhu, S. Murali, M.D. Stoller, and R.S. Ruoff, ACS Nano **5**, 3333 (2011).

40. J. Zhang and X.S. Zhao, J. Phys. Chem. C **116**, 5420 (2012).

41. J.M. Mativetsky, E. Treossi, E. Orgiu, M. Melucci, G.P. Veronese, P. Samorì, and V. Palermo, J. Am. Chem. Soc. **132**, 14130 (2010).

42. J. Lee, K.S. Novoselov, and H.S. Shin, ACS Nano **5**, 608 (2011).

43. J. Li and C. Liu, Eur. J. Inorg. Chem. **2010**, 1244 (2010).

44. J. Liang, L. Li, K. Tong, Z. Ren, W. Hu, X. Niu, Y. Chen, and Q. Pei, ACS Nano **8**, 1590 (2014).

45. I.N. Kholmanov, S.H. Domingues, H. Chou, X. Wang, C. Tan, J.-Y. Kim, H. Li, R. Piner, A.J.G. Zarbin, and R.S. Ruoff, ACS Nano **7**, 1811 (2013).

46. S. Hunter and T.D. Anthopoulos, Adv. Mater. **25**, 4320 (2013).

47. S. Hunter, J. Chen, and T.D. Anthopoulos, Adv. Funct. Mater. **24**, 5969 (2014).

48. F. Giannazzo, I. Deretzis, A. La Magna, F. Roccaforte, and R. Yakimova, Phys. Rev. B **86**, 235422 (2012).

49. F. Giannazzo, G. Fisichella, A. Piazza, S. Agnello, and F. Roccaforte, Phys. Rev. B **92**, 081307 (2015).

50. C. Gómez-Navarro, R.T. Weitz, A.M. Bittner, M. Scolari, A. Mews, M. Burghard, and K. Kern, Nano Lett. **7**, 3499 (2007).

51. K. Maize, S. R. Das, S. Sadeque, A. M. S. Mohammed, A. Shakouri, D. B. Janes, and M. A. Alam, Applied Physics Letters **106**, 143104 (2015).

52. T. Kim, A. Canlier, G.H. Kim, J. Choi, M. Park, and S.M. Han, ACS Appl. Mater. Interfaces **5**, 788 (2013).

(a)


50 μm

(b)

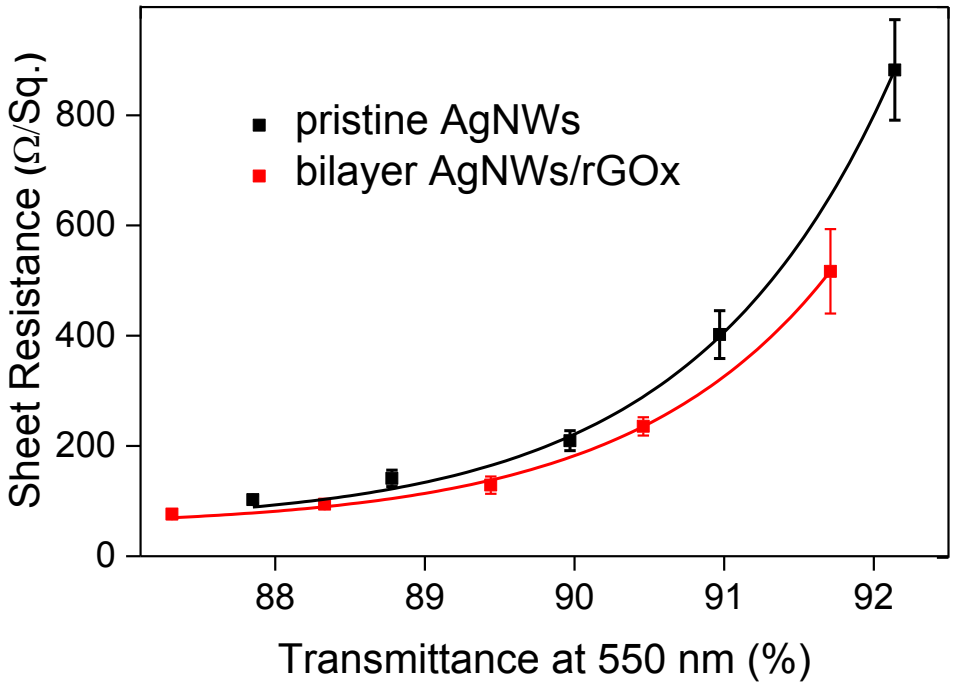
pristine AgNWs
bilayer AgNWs/rGOx
Sheet Resistance (Ω/Sq.)
0
200
400
600
800
88
89
90
91
92
Transmittance at 550 nm (%)

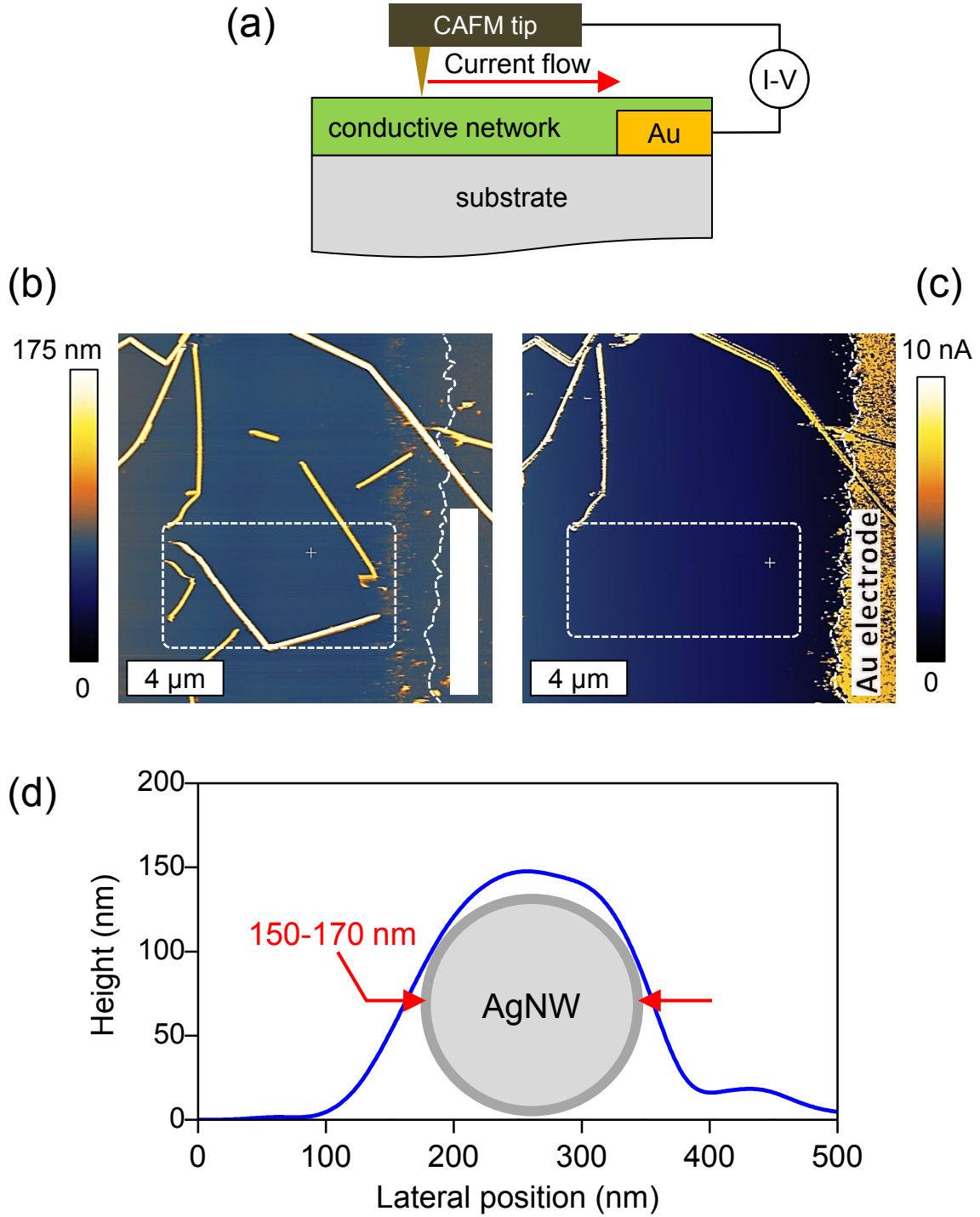
(a)
CAFM tip
Current flow
I-V
conductive network
Au
substrate
(b)
175 nm
0
4 μm
(c)
10 nA
0
Au electrode
4 μm
(d)
Height (nm)
200
150
100
50
0
150-170 nm
AgNW
0
100
200
300
400
500
Lateral position (nm)

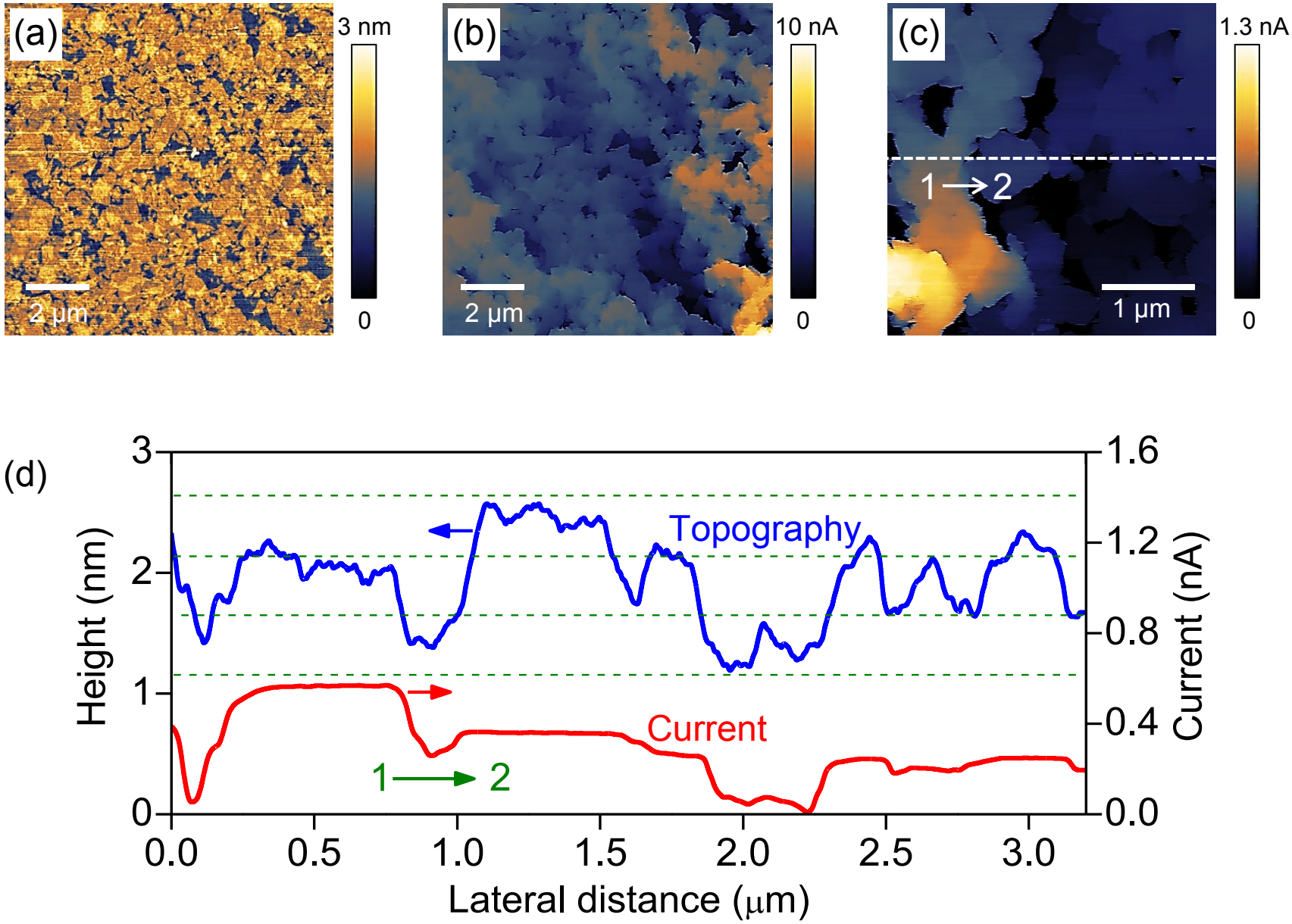
(a)
3 nm
0
2 μm
(b)
10 nA
0
2 μm
(c)
1.3 nA
0
1 → 2
1 μm
(d)
Height (nm)
Current (nA)
Topography
Current
1 → 2
Lateral distance (μm)
0
1
2
3
0.0
0.4
0.8
1.2
1.6
0.0
0.5
1.0
1.5
2.0
2.5
3.0

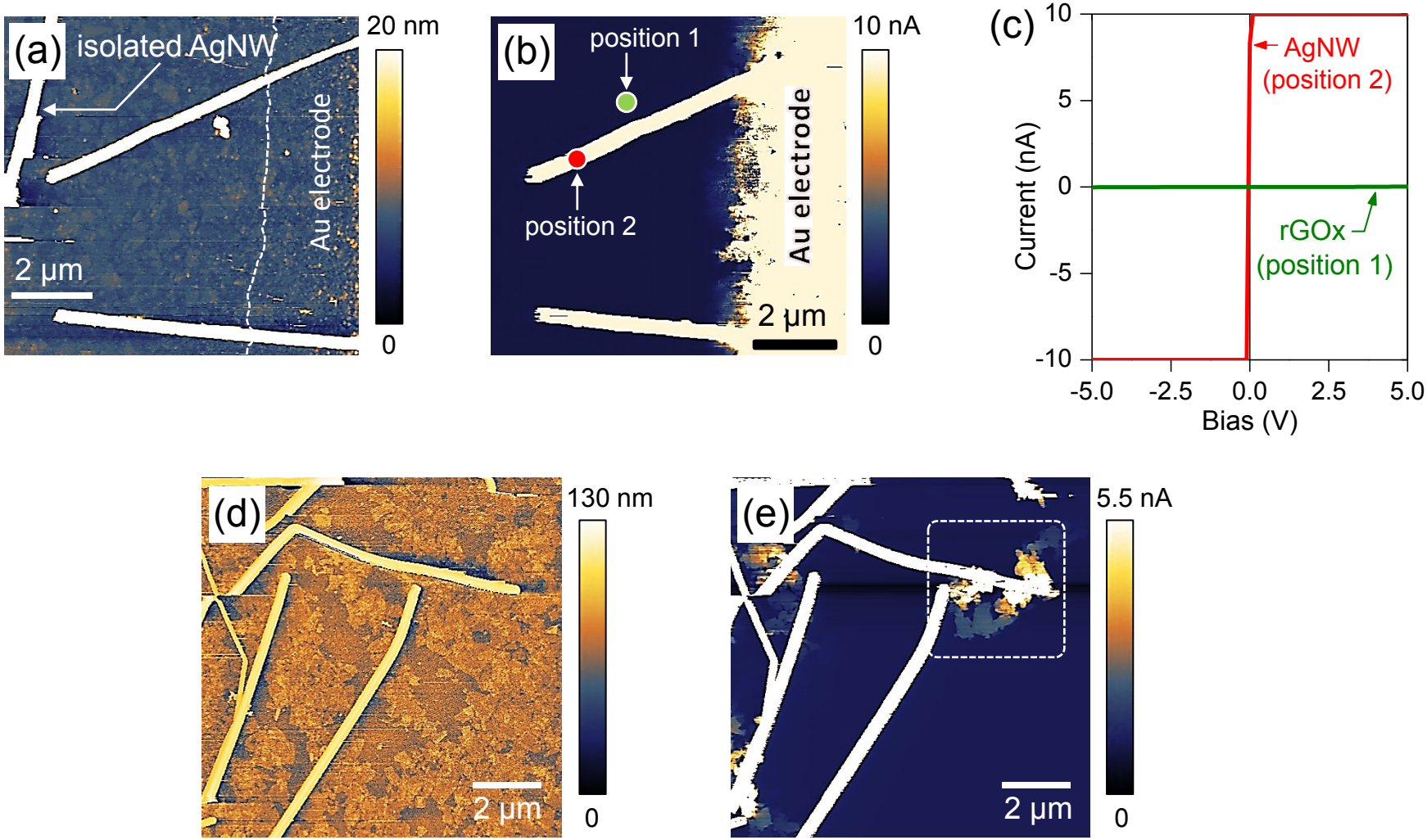
(a)
isolated AgNW
Au electrode
2 μm
20 nm
0
(b)
position 1
position 2
Au electrode
2 μm
10 nA
0
(c)
AgNW
(position 2)
rGOx
(position 1)
Current (nA)
Bias (V)
10
5
0
-5
-10
-5.0
-2.5
0.0
2.5
5.0
(d)
2 μm
130 nm
0
(e)
2 μm
5.5 nA
0

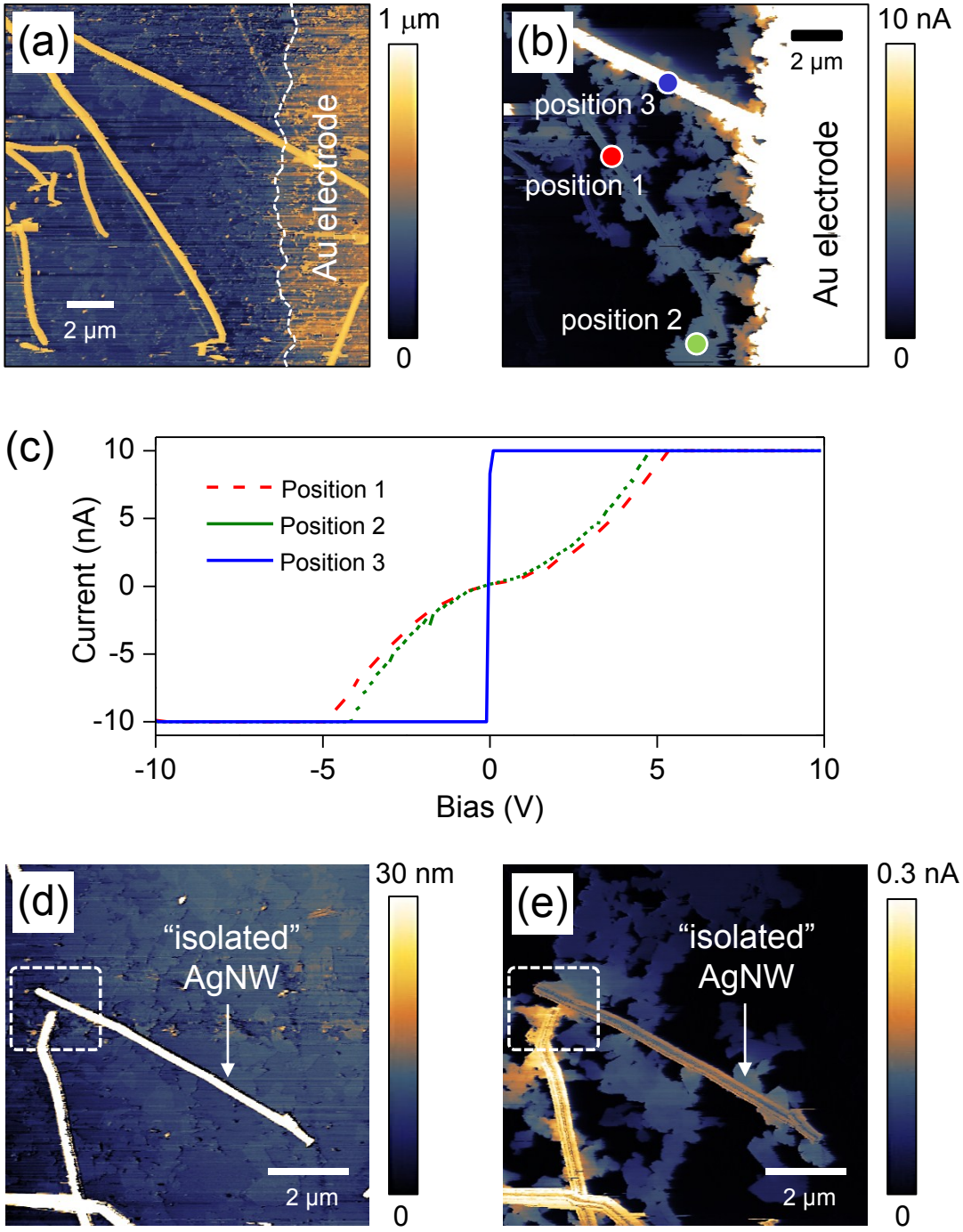
(a)
1 μm
0
Au electrode
2 μm
(b)
10 nA
0
2 μm
position 3
position 1
position 2
Au electrode
(c)
Current (nA)
10
5
0
-5
-10
Position 1
Position 2
Position 3
-10
-5
0
5
10
Bias (V)
(d)
30 nm
0
"isolated"
AgNW
2 μm
(e)
0.3 nA
0
"isolated"
AgNW
2 μm

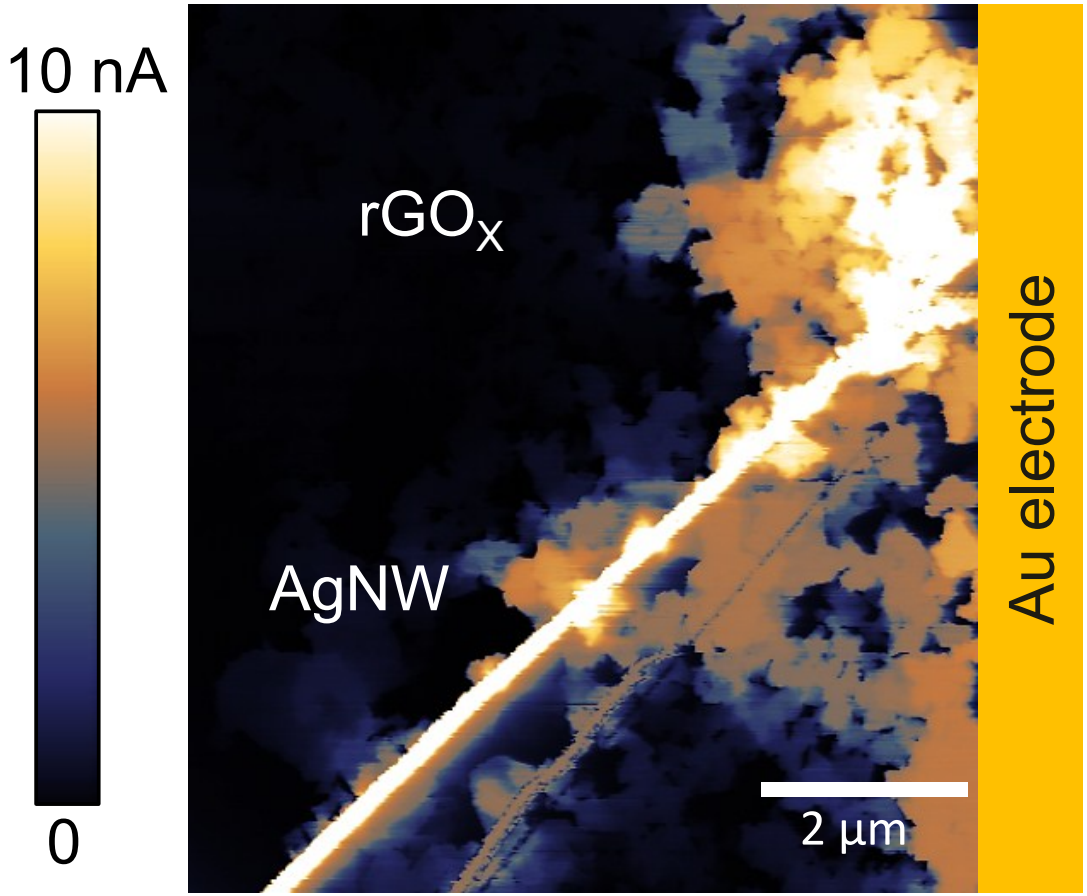
10 nA
0
rGO$_X$
AgNW
2 µm
Au electrode